Journal of Glaciology (2017), **63**(240) 629–636 doi: 10.1017/jog.2017.28

Acquisition of a 3 min, two-dimensional glacier velocity field with terrestrial radar interferometry

DENIS VOYTENKO,[1] TIMOTHY H. DIXON,[2] DAVID M. HOLLAND,[1] RYAN CASSOTTO,[3] IAN M. HOWAT,[4] MARK A. FAHNESTOCK,[5] MARTIN TRUFFER,[5] SANTIAGO DE LA PEÑA[4]

[1]*Courant Institute of Mathematical Sciences, New York University, New York, NY, USA*
[2]*School of Geosciences, University of South Florida, Tampa, FL, USA*
[3]*Department of Earth Sciences, University of New Hampshire, Durham, NH, USA*
[4]*School of Earth Sciences and Byrd Polar Research Center, The Ohio State University, Columbus, OH, USA*
[5]*Geophysical Institute, University of Alaska Fairbanks, Fairbanks, AL, USA*
Correspondence: Denis Voytenko <denis.voytenko@nyu.edu>

ABSTRACT. Outlet glaciers undergo rapid spatial and temporal changes in flow velocity during calving events. Observing such changes requires both high temporal and high spatial resolution methods, something now possible with terrestrial radar interferometry. While a single such radar provides line-of-sight velocity, two radars define both components of the horizontal flow field. To assess the feasibility of obtaining the two-dimensional (2-D) flow field, we deployed two terrestrial radar interferometers at Jakobshavn Isbrae, a major outlet glacier on Greenland's west coast, in the summer of 2012. Here, we develop and demonstrate a method to combine the line-of-sight velocity data from two synchronized radars to produce a 2-D velocity field from a single (3 min) interferogram. Results are compared with the more traditional feature-tracking data obtained from the same radar, averaged over a longer period. We demonstrate the potential and limitations of this new dual-radar approach for obtaining high spatial and temporal resolution 2-D velocity fields at outlet glaciers.

KEYWORDS: glacier flow, glacier geophysics, glaciological instruments and methods

1. INTRODUCTION

Velocity fields of tidewater glaciers are sensitive indicators of the various driving and resisting forces acting upon them (e.g. Howat and others, 2008). Unfortunately, it is challenging to obtain such data with adequate spatial and temporal resolution. Discrete GPS measurements undersample the velocity field in a spatial sense. Satellite observations give a well-resolved two-dimensional (2-D) (horizontal) velocity field via feature or speckle tracking (e.g. Joughin and others, 2008; Ahn and Howat, 2011) but undersample the temporal variation. Temporal resolution of ice velocity from space-borne sensors is generally limited to several days or more and thus undersamples short-term fluctuations in the highly dynamic zones of marine-terminating glaciers, where iceberg calving and changes in basal water pressure may be frequent and lead to rapid stress and velocity variations.

Jakobshavn Isbrae is an outlet glacier on the west coast of Greenland (Fig. 1). The main trunk of the glacier is ~5 km wide and moves at ~40 m d^{-1} (Amundson and others, 2010) with cliff heights of ~100 m (Xie and others, 2016). Jakobshavn drains ~6% of the Greenland ice sheet (Bindschadler, 1984) and is likely to have accounted for ~4% of the increase in sea-level rise rate for the 20th century (Houghton and others, 2001). It represents an important target for research aimed at understanding the overall health of the Greenland ice sheet.

Terrestrial radar interferometers (TRIs) have been used to study a variety of geophysically deforming surfaces at very high (minute-scale) sampling rates. Caduff and others (2015) and Voytenko and others (2015a) review the basic TRI technique. Voytenko and others (2015c) used near-field TRI observations to resolve the vertical component of deformation along a tidewater glacier terminus. Xie and others (2016) observed a calving event at Jakobshavn using a TRI. Feature-tracking techniques have been applied to TRI observations of Jakobshavn's proglacial fjord (Peters and others, 2015). However, such techniques have limited temporal resolution compared with interferometric measurements (hour vs minute-scale) or require very fast motion (e.g. ice mélange during a calving event). Although a single instrument provides only scalar line-of-sight (LOS) measurements, in principle, measurements from two identical synchronized TRIs positioned at different locations but observing a common overlapping area can be combined to define both horizontal components of glacier velocity.

In this study, our TRIs are real-aperture Ku band (1.74 cm wavelength) GAMMA Portable Radar Interferometers (GPRI) (Werner and others, 2008). Each instrument has three antennas (one transmitting and two receiving). The receiving antennas have a 25 cm baseline, and the transmitting and lower receiving antenna (which are the ones used in this study) have a 60 cm baseline, which allow for displacement sensitivity of ~1 mm and an elevation sensitivity of 3 m at a distance of 2 km (Strozzi and others, 2012). The antennas are attached to a rotating frame and scan an arc of a specified angle to image the scene. The maximum range of our TRIs is ~16 km, with a nominal range resolution of 0.75 m and an azimuth resolution of 7 m at 1 km, which linearly widens with distance. TRIs are designed for installation on stable bedrock. Deployments on moving ice are logistically

https://doi.org/10.1017/jog.2017.28 Published online by Cambridge University Press

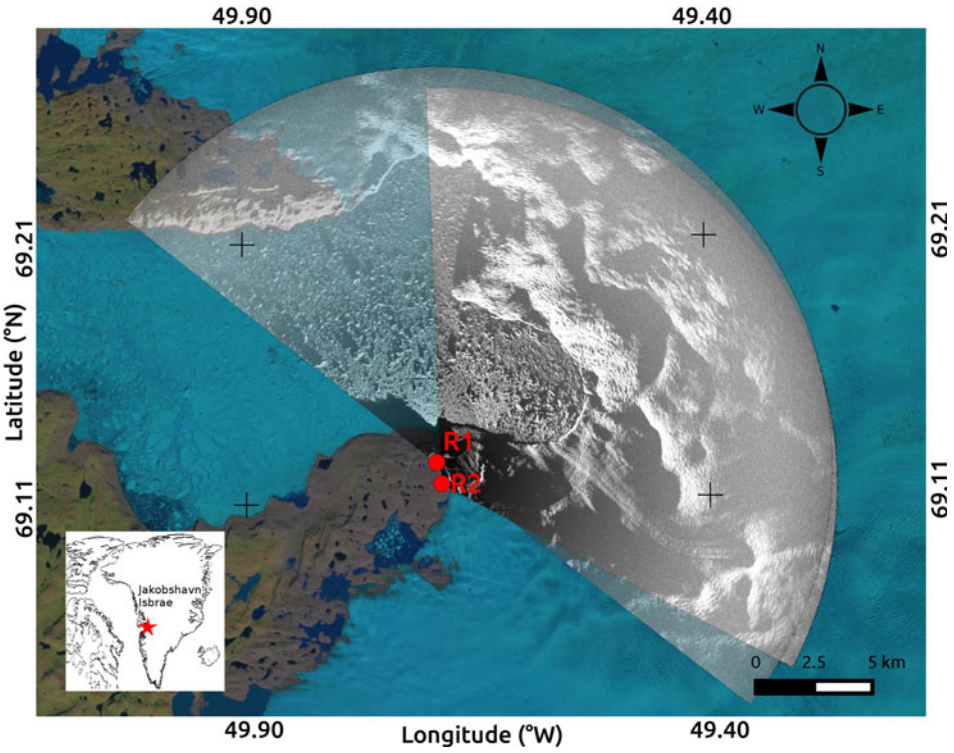

Fig. 1. Map of the field area. Site location relative to Greenland marked by red star (inset). *R*1 and *R*2 show the locations of the TRI instruments. Their respective coverage areas are shown by overlapping gray scales, overlain on a LANDSAT image from 11 August 2014 (obtained from landsatlook.usgs.gov).

difficult, complicate the measurements, and thus are not ideal. Because the TRI does not move in space during a study period, no topographic phase correction is required when processing the interferograms.

Methods to obtain components of motion from two viewpoints have been developed for weather radars (Lhermitte and Miller, 1970) and subsequently for satellite synthetic aperture radar data from ascending and descending passes (Joughin and others, 1998; Fialko and others, 2005). Here, we present a similar TRI-based approach to resolve the two horizontal components of the surface velocity field at Jakobshavn.

2. METHODS

2.1. Derivation of equations to combine data from two radars

Consider a parcel of glacier ice that is moving in two dimensions and is seen by two radars (TRIs). Assume that the vertical motion is insignificant. The components of the velocity vector of the parcel with respect to east and north are V_x and V_y. The TRI, however, only measures the velocity of the parcel in the direction of its LOS, with V_{R1} representing the LOS velocity measured by TRI 1, and V_{R2} representing the LOS velocity measured by TRI 2. The LOS angles (measured counterclockwise from east by convention) for each azimuth line are θ_1 and θ_2 for TRIs 1 and 2, respectively (Fig. 2).

We derive an equation describing the measured LOS velocity as a function of V_x and V_y of the parcel and the LOS angle of the TRI, θ. We do this by rotating the coordinate system of a given vector $[V_x, V_y]$ by the angle θ.

$$\begin{bmatrix} V'_x \\ V'_y \end{bmatrix} = \begin{bmatrix} \cos(\theta) & \sin(\theta) \\ -\sin(\theta) & \cos(\theta) \end{bmatrix} \begin{bmatrix} V_x \\ V_y \end{bmatrix}. \quad (1)$$

Note that V'_x is the component of velocity in the direction of the unit vector given by θ, which happens to be the velocity component measured by the TRI. Since this is the only component measured by the TRI, we can ignore the other component of rotation (V'_y), and obtain an equation for the measured radial velocity:

$$V_R = V_x\cos(\theta) + V_y\sin(\theta). \quad (2)$$

Therefore, the velocity equations for both TRIs are:

$$V_{R1} = V_x\cos(\theta_1) + V_y\sin(\theta_1), \quad (3)$$

$$V_{R2} = V_x\cos(\theta_2) + V_y\sin(\theta_2). \quad (4)$$

The above equations are sufficient to generate a forward model for the dual TRI velocity problem.

In reality, the two TRIs measure V_{R1} and V_{R2}, where θ_1 and θ_2 are the instrument look angles, and are known from the locations of the instruments and the georeferenced images. The focused TRI images are by default in polar coordinates, where one axis is azimuth (an angular measure of the scan) and the other is slant range (distance from the origin, measured as the shortest distance from radar to target). Therefore, we can rewrite the TRI velocity equations in the $A\mathbf{x} = \mathbf{b}$ form, and solve for V_x and V_y for each point using matrix inversion.

$$\begin{bmatrix} V_x \\ V_y \end{bmatrix} = \begin{bmatrix} \cos(\theta_1) & \sin(\theta_1) \\ \cos(\theta_2) & \sin(\theta_2) \end{bmatrix}^{-1} \begin{bmatrix} V_{R1} \\ V_{R2} \end{bmatrix}. \quad (5)$$

https://doi.org/10.1017/jog.2017.28 Published online by Cambridge University Press

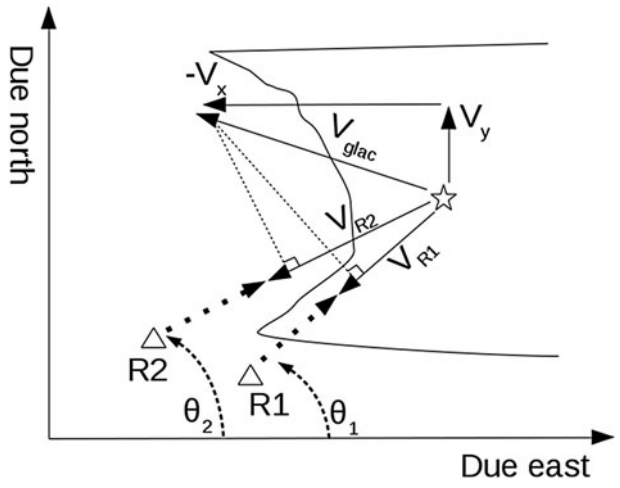

Fig. 2. Diagram of the field set-up for the derivation of Eqn (1). Radar positions are *R*1 and *R*2 (triangles), LOS velocities measured with each radar are V_{R1} and V_{R2}, angles from the radars to a parcel of interest on the glacier (stars) are θ_1 and θ_2 (dashed lines). True velocity of an ice parcel observed by the radar on the glacier is V_{glac}, and its north and east components are V_y and V_x. Vectors of the radars are given by the dotted lines originating from radars toward the parcel of interest. V_x and V_y are obtained using the measured V_{R1} and V_{R2} and the known (from the instrument locations) θ_1 and θ_2. Note that the LOS velocities (V_{R1} and V_{R2}) are obtained from a vector projection of V_{glac} onto the look vectors of *R*1 and *R*2. Also note that if the glacier is moving toward the radar, the measured velocity is negative because the distance (slant range) is decreasing between the first and second image in the interferogram.

The inverse matrix can be written explicitly with no numerical inversion required:

$$A^{-1} = \frac{1}{det(A)} \begin{bmatrix} \sin(\theta_2) & -\sin(\theta_1) \\ -\cos(\theta_2) & \cos(\theta_1) \end{bmatrix}, \quad (6)$$

where $det(A) = [\cos(\theta_1)\sin(\theta_2) - \sin(\theta_1)\cos(\theta_2)] = \sin(\theta_2 - \theta_1)$.

2.2. Data acquisition and processing

We set up two TRI instruments on the south side of the Ilulissat fjord ~6 km from the terminus of Jakobshavn Isbrae (Fig. 1) and collected data with a 3 min sampling interval. The radar separation was ~1 km, constrained by local geography. One radar was at an elevation of 314 m and the other one was at 270 m. A built-in GPS receiver provides accurate clock information to the TRI. Because of the 3 min sampling rate, we set the acquisition start times on both instruments to be the same (as opposed to being offset by 1 or 2 min). We use a single acquisition pair (2012/08/01 20:01 and 2012/08/01 20:04) to demonstrate the concept of our method, and compare the results with a longer 3-day period (2012/07/31 16:05 to 2012/08/03 16:06) of motion derived by feature tracking.

We prepare the interferograms from non-resampled single-look complex files using the GAMMA software package. During processing, we multilook (spatially average) the TRI data by 12 looks (averaged pixels) in range, smooth the interferograms with an adaptive filter (Goldstein and Werner, 1998), set a phase unwrapping mask focused on the stationary rocks and the main trunk of the glacier (ignoring the ice mélange), and unwrap the phase using a minimum cost flow algorithm. We then convert the unwrapped interferograms (and the multilooked intensity images) into rectangular coordinates with 15 m pixel spacing. This conversion is needed for georeferencing to properly define the angles relative to due east. Due to the small elevation differences between the TRIs and the glacier (~200 m over a horizontal distance of ~5 km, suggesting an incidence angle of ~2°), we do not perform a terrain correction for conversion from slant range to ground range. The interferograms are then converted into velocities via a multiplicative factor of $-\lambda/4\pi\Delta t$, where λ is the wavelength (1.74 cm for the GPRI) and Δt is the time between the images in the interferogram (3 min in our case).

One of the radar datasets suffers from phase unwrapping issues, likely due to the look direction of the radar relative to the principal direction of glacier motion and the 3 min sampling rate. We correct for this by manually adjusting the resulting unwrapped interferogram by two cycle slips and recalculating the velocity (this offset is determined by examining an area where the look angles of both radars are similar, and should measure similar rates). The intensity images are then compared with LANDSAT images and adjusted 39° and 59° for rotational offsets related to instrument locations, allowing for accurate calculation of the horizontal viewing angle. These offsets are determined by iteratively adjusting a rotation angle of a georeferenced image until some salient features (typically rock outcrops) visually overlap with the same features in a LANDSAT image. After georeferencing both velocity datasets to the same image space, we calculate θ_1 and θ_2 for each overlapping pixel using the radar pixel coordinates and the pixel coordinates containing the velocity values measured by each radar, and solve for the east and north components of velocity using Eqn (5) and the analytically derived inverse matrix in Eqn (6).

We use the correlation-based OpenPIV (particle image velocimetry) package (Taylor and others, 2010) to measure offsets over a 3-day period from the TRI images to compare our results. Here, the georeferenced intensity images have 5 m pixel spacing with a search window of 64 pixels and an overlap of 32 pixels. The output of each velocity component is smoothed with a 5-pixel median filter. We then resample the resulting interferometric velocity component maps to the dimensions of the feature-tracking data and smooth them with a 5-pixel median filter for comparison (Figs 3, 4).

We combine the above method with a Monte Carlo simulation to perform uncertainty analysis, offering a more convenient alternative to error propagation (which would require calculating partial derivatives). The Monte Carlo method (Fig. 5) estimates the probability distribution of the solution by repeatedly solving the equations by sampling from the known or, more commonly, assumed probability distributions of the input parameters. Here, these are the radar LOS velocities, their orientations and their respective standard deviations (SDs). A large enough number of runs are performed to generate meaningful distribution statistics. Here, the results are the velocity components, where each component has its own probability distribution with a mean and SD.

We assume that there are no phase unwrapping errors (from inspection and after accounting for the offset mentioned earlier) and that the radar-derived velocity and angle values are normally distributed with SDs of 0.5 m d^{-1} derived from on-rock TRI measurements at Breiðamerkurjökull (Voytenko

https://doi.org/10.1017/jog.2017.28 Published online by Cambridge University Press

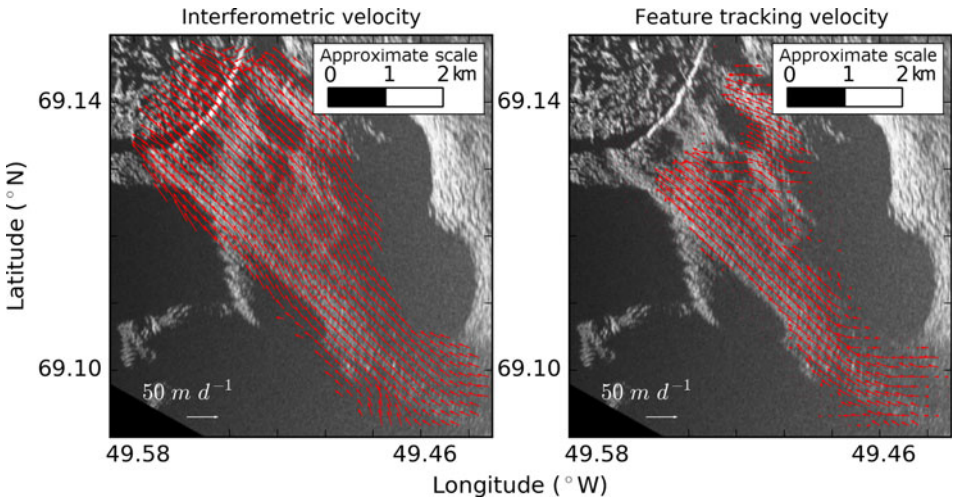

Fig. 3. Plots of ice velocity derived from the 3 min interferometric data pair (left) and the 3-day feature tracking (right). The velocity magnitudes and directions are similar. The feature-tracking data are truncated near the terminus due to a calving event.

and others, 2015b) and 0.1° (the smallest eye-detectable difference when manually georeferencing the TRI image to a background LANDSAT image; the TRI azimuth positioner errors are negligible), respectively. We then run a simulation with 1000 samples for every measurement point and calculate the resulting 'average' velocity (in a probabilistic sense) along with an uncertainty (SD) for each component (Fig. 6). We then use the resulting data to obtain the best estimate and uncertainty of the principal direction of glacier motion (azimuth, given by $90^\circ - \arctan(V_y/V_x)$) and the velocity magnitude (given by $(V_x^2 + V_y^2)^{1/2}$) (Fig. 7).

Since our method involves matrix inversion, we also need to consider precision loss due to the conditioning of the system (Atkinson, 2008). The condition number (κ) represents the orthogonality of the system (a high condition number implies that the vectors inside the matrix are not orthogonal and that a small perturbation of the inputs will result in a large change in the outputs). A condition number of 1 implies orthogonality. We use the condition number of A, the matrix to be inverted (see the matrix of coefficients in Eqns (5) and (6)), and an L_2 norm to estimate precision loss for our 2-D velocity results. Note that the matrix only depends on the orientation of the two radars (i.e. the instrument locations and not the actual velocity measurements). In our case, A is ill conditioned when the look angles of the TRIs are similar.

$$\kappa = \|A\|_2 \|A^{-1}\|_2. \tag{7}$$

Following the equation below, we calculate C, the number of digits of precision loss.

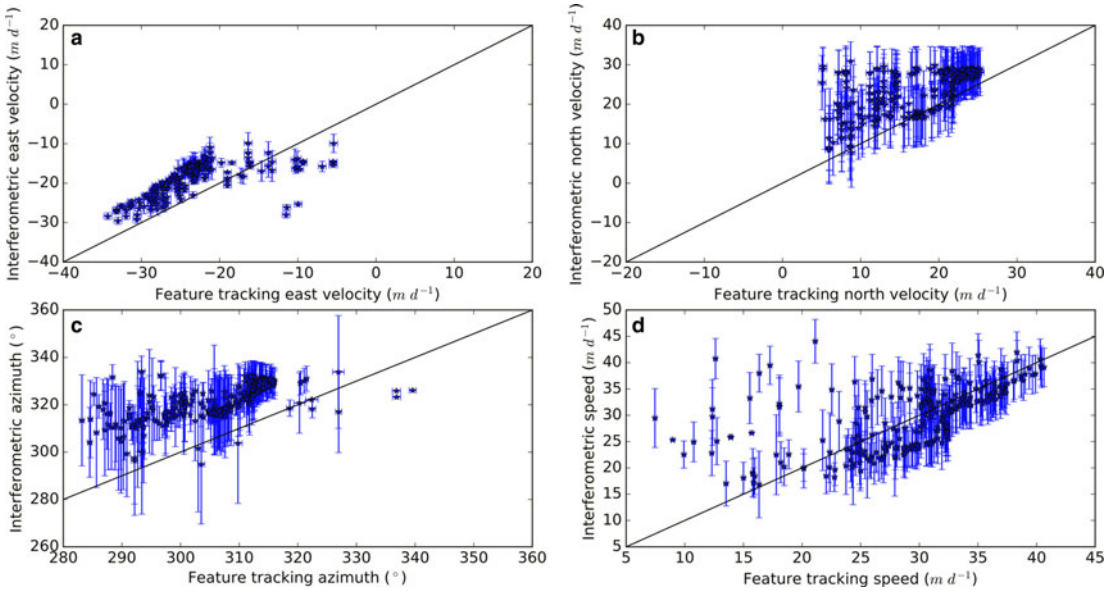

Fig. 4. A pointwise comparison between the overlapping 2-D interferometric and feature-tracking data for components >5 m d^{-1}. The plots compare eastward velocity (a), northward velocity (b), azimuth (c) and velocity magnitude (d). One-to-one relationship lines are shown on every plot. Note that the variability is close to what is described by the Monte Carlo simulation (Figs 6, 7). Error bars show the one SD uncertainties for the interferometric data. The feature-tracking (PIV) uncertainty is assumed to be 0.1 pixels (Huang and others, 1997), which, in this case, is 0.2 m d^{-1} (0.5 m over a 3-day period, to one significant figure) for each of the velocity components. The feature-tracking uncertainty error bars for the magnitude and azimuth are derived from another Monte Carlo simulation.

https://doi.org/10.1017/jog.2017.28 Published online by Cambridge University Press

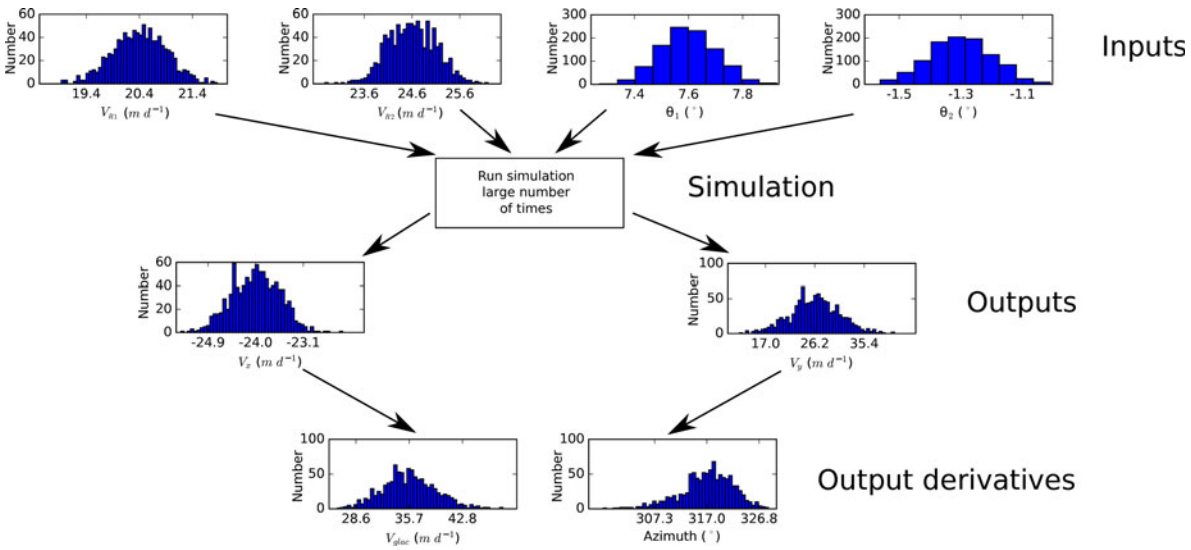

Fig. 5. A visual example of a Monte Carlo simulation (1000 runs) for a single point on the glacier surface. Here, the inputs are the radar velocity measurements (V_{R1} and V_{R2}) and their respective view directions (θ_1 and θ_2). Note that we only obtain the distributions of V_x and V_y using the simulation. We then calculate the azimuth and velocity magnitude along with their respective uncertainties from the results of the simulation. This process is repeated for every desired data point over the glacier surface to produce Figures 6, 7.

$$C = \log_{10} \kappa. \tag{8}$$

3. RESULTS AND DISCUSSION

Most of the ice around the study area flows to the northwest with an azimuth of ~315° and uncertainties (one SD) of ± 5° close the terminus and up to ±15° further up-glacier with velocity magnitudes ranging from ~50 m d^{-1} near the ice front to ~25 m d^{-1} up-glacier with uncertainties ~ ±6 m d^{-1} (Figs 3, 6, 7). The Monte Carlo simulation suggests that east-west uncertainties are ~1 m d^{-1}, while north-south uncertainties are ~6 m d^{-1} (Fig. 6). This is likely due to the positioning of the radars relative to the main trunk of the glacier, their limited spatial separation (constrained by our site) and the scan orientations.

The interferometric and feature-tracking techniques yield similar magnitudes and directions (Fig. 4), except for slight

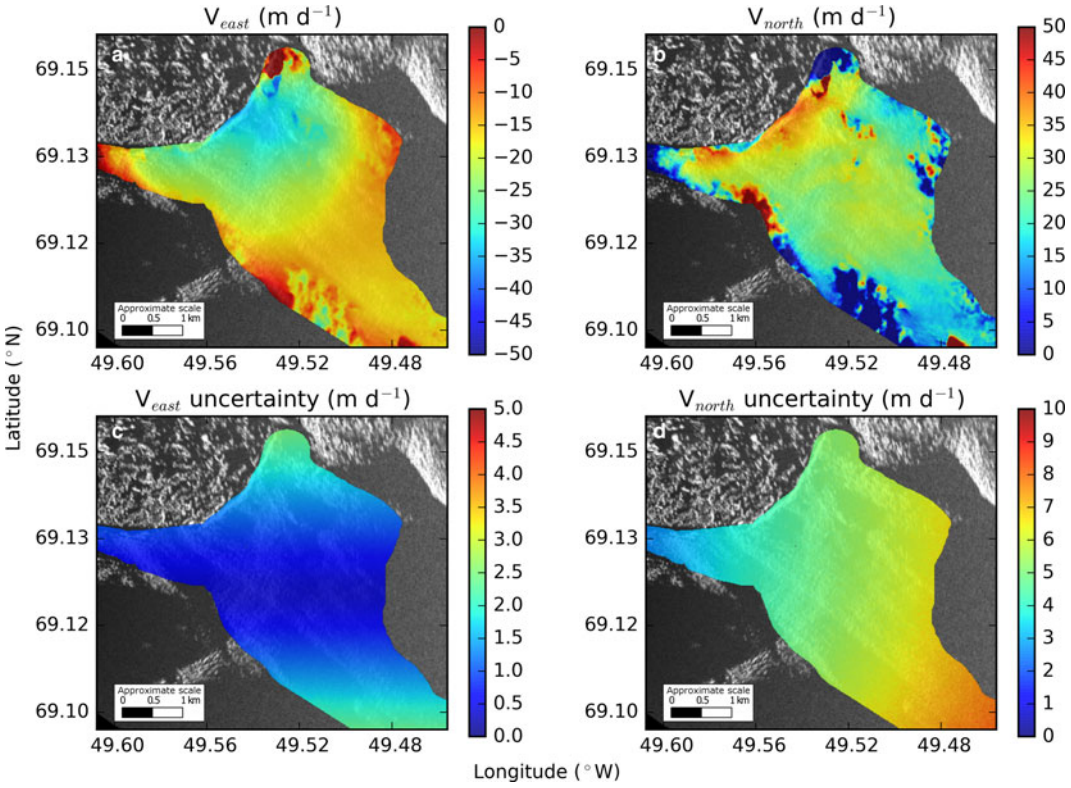

Fig. 6. East (a) and north (b) velocity component maps and their uncertainties derived from interferometry and the Monte Carlo simulation. Note that northward uncertainties (d) are higher than eastward uncertainties (c), likely due to the scan orientations of the two TRIs.

https://doi.org/10.1017/jog.2017.28 Published online by Cambridge University Press

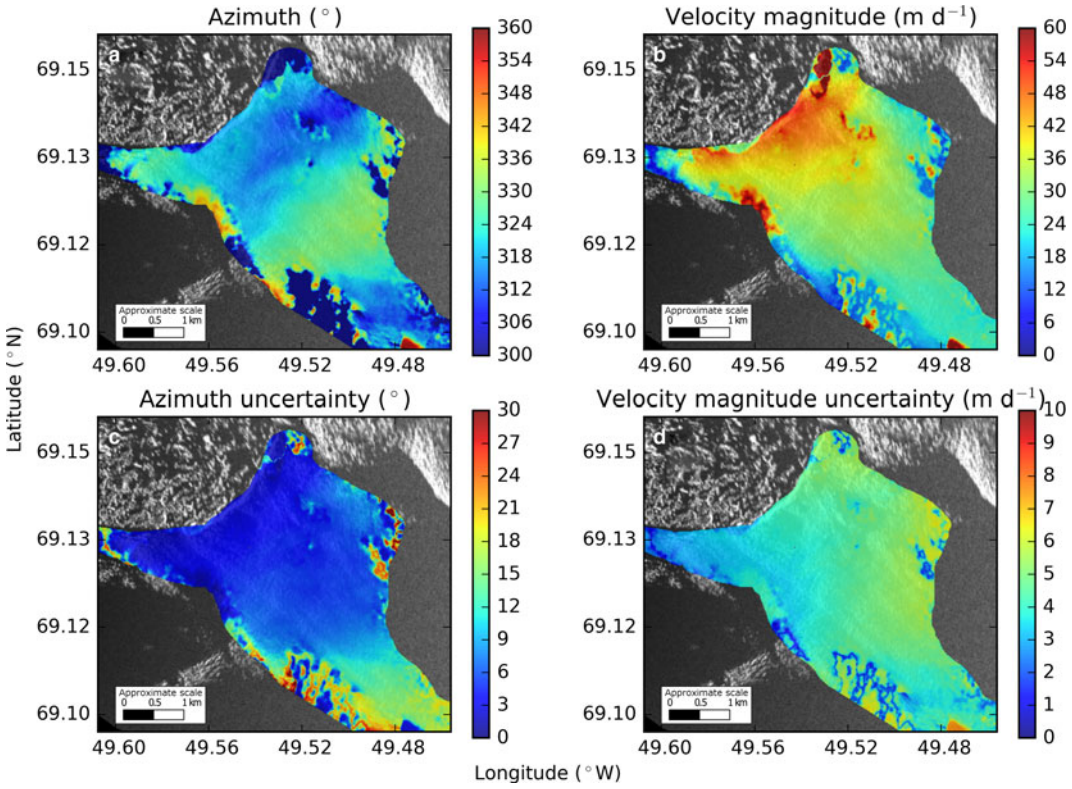

Fig. 7. Direction and velocity magnitudes derived from interferometry (a, b) and their respective uncertainties (c, d) are all calculated from the Monte Carlo simulation. Note that azimuth is defined to be positive clockwise from north.

discrepancies in the direction of motion where interferometric azimuth is systematically ~15° greater than the feature-tracking azimuth. This may be due to different sampling periods, measurement uncertainties and the conditioning of the equations. Additionally, the interferometric results are based on a 3 min period, while the feature-tracking results cover a 72 h period and include a calving event, which could affect the average direction of ice motion and its velocity magnitude (Amundson and others, 2008; Nettles and others, 2008).

We also use the Monte Carlo simulation results to plot error ellipses (covering two SDs) for a selected subset of points (Fig. 8). The method of plotting the error ellipses depends on the uncertainty of each component (in this case, obtained from the Monte Carlo simulations) and a desired confidence interval for the ellipse and is described in detail by Haug (2012) and Voytenko and others (2015b). Note that the shape of the error ellipses agrees with the uncertainties presented in Figure 6.

While examining the condition number of the system of equations, we note that when C is 10, we lose one digit of precision. Considering our previous velocity measurement uncertainty assumption of ±0.5 m d^{-1} (i.e. our measurements are precise to the ones decimal place), losing one decimal place of precision means that the resulting velocity is only accurate to the tens decimal place, or ±5 m d^{-1}.

Given our instrument locations, most of the terminus loses a little over one digit of precision (Fig. 9), suggesting uncertainties of at least 5 m d^{-1} for each component, which are more conservative than the uncertainties computed from the Monte Carlo simulation (~1 to ~6 m d^{-1}) (Fig. 6).

At Jakobshavn, locations for both radars that would be optimal for this method are either covered with glacier ice or are close to 16 km away from the terminus (near the useful range of the instrument), making 2-D interferometric measurements with TRI challenging at this location. However, since these precision loss calculations only depend on the instrument locations, they can be used in a forward model prior to future deployments to determine suitable instrument positions at other sites. For applications

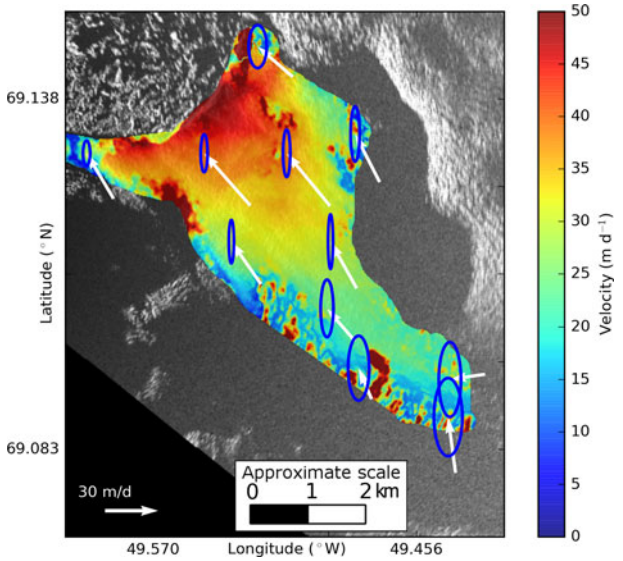

Fig. 8. Plot of error ellipses for a selected subset of points over the glacier surface overlain on a map of velocity magnitude derived from interferometry. The ellipses (blue) cover two SDs and are scaled relative to the arrows (white) showing the direction of motion and speed. Note that the north uncertainty is much greater than the east uncertainty.

https://doi.org/10.1017/jog.2017.28 Published online by Cambridge University Press

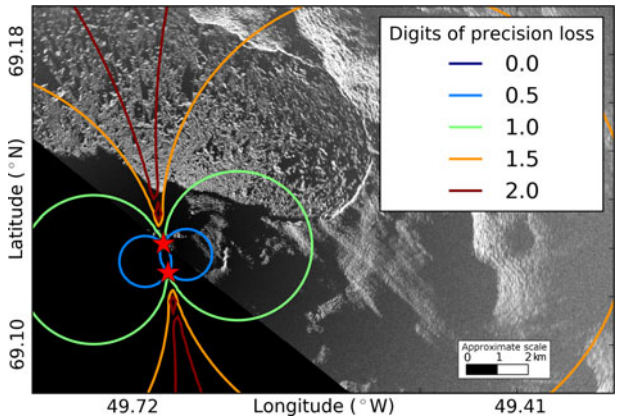

Fig. 9. Contours of loss of digits of precision considering the positions of the two radars (red stars) calculated from the condition number of the matrix of coefficients in Eqns (5) and (6). Most of the terminus experiences between 0.5 and 1.5 digits of loss.

involving imaging the calving front of marine-terminating glaciers, if geography and logistics allow, the optimum radar separation should be such that the two radars are imaging the target area at close to right angles (to improve the conditioning of the system of equations) and within the operating range of the instruments.

4. CONCLUSIONS

Our work shows that it is possible to obtain minute-scale 2-D velocity fields using TRI. Although feature tracking can be used to obtain 2-D velocity fields from pairs of intensity images from a single radar, the results are likely to cover multiple hours of motion. Instead, our algorithm can be used to obtain results over minute-scale time steps using two radars. This method should be applicable in any location where a favorable site geometry exists. Salient features (e.g. bare rocks), which are visible in the TRI and the background (e.g. LANDSAT) imagery, are also required for visual georeferencing.

Based on results from our deployment and the analysis presented above, we can define an improved experiment design that should yield a robust 2-D glacier velocity field in most situations.

First, the two radars should be spatially separated by an amount such that there is sufficient angular separation for most of their overlapping image areas. Optimal radar placement can be determined before field deployment by modeling radars at different locations and calculating the expected precision loss via the condition number. Ideally, the radar look directions should be perpendicular over the region of interest, the area of which should be well within the ~16 km operating range.

Second, the time interval between radar scans, which should be identical for the two instruments, should be sufficiently short such that phase unwrapping can be done accurately (as close as possible to yield a displacement of half of a wavelength, while letting the radar scan a large enough arc to cover the area of interest). For fast moving glaciers such as Jakobshavn, 1½–2 min TRI scans may be optimum. In our 2012 experiment, we used 3 min scans. This longer time scan may have contributed to some of the phase unwrapping problems we encountered.

Having frequent and spatially dense coverage of 2-D glacier surface velocities at the terminus is necessary to improve our understanding of the calving process. Since GPS deployments on rapidly moving ice are logistically difficult, costly and sparse, and satellite measurements do not have minute-scale revisit times, a combination of two TRI instruments can provide the necessary spatial and temporal resolution.

ACKNOWLEDGEMENTS

We thank editor Hamish Pritchard, Reinhard Drews and an anonymous reviewer for their valuable comments. We thank the Gordon and Betty Moore Foundation and NASA's Cryospheric Sciences program. T.H.D. acknowledges support from NASA grant NNX12AK29G. R.C. acknowledges support under the NASA Earth and Space Science Fellowship (NNX14AL29H). D.M.H. and D.V. acknowledge support of NYU Abu Dhabi Research Institute grant G1204, as well as from NASA through the 'Oceans Melting Greenland' program led by JPL with subcontract to NYU and thank support from NSF Polar Programs ARC-1304137.

REFERENCES

Ahn Y and Howat IM (2011) Efficient automated glacier surface velocity measurement from repeat images using multi-image/multi-chip and null exclusion feature tracking. *IEEE Trans. Geosci. Remote Sens.*, **49**(8), 2838–2846

Amundson J and 5 others (2008) Glacier, fjord, and seismic response to recent large calving events, Jakobshavn Isbræ, Greenland. *Geophys. Res. Lett.*, **35**(22)

Amundson JM and 5 others (2010) Ice mélange dynamics and implications for terminus stability, Jakobshavn Isbræ, Greenland. *J. Geophys. Res.: Earth Surf.*, **115**(F1)

Atkinson KE (1989) *An introduction to numerical analysis* 2nd Edn. John Wiley & Sons, New York

Bindschadler RA (1984) Jakobshavns Glacier drainage basin: a balance assessment. *J. Geophys. Res.: Oceans* (1978–2012), **89** (C2), 2066–2072

Caduff R, Schlunegger F, Kos A and Wiesmann A (2015) A review of terrestrial radar interferometry for measuring surface change in the geosciences. *Earth Surf. Process. Landf.*, **40**(2), 208–228

Fialko Y, Sandwell D, Simons M and Rosen P (2005) Three-dimensional deformation caused by the Bam, Iran, earthquake and the origin of shallow slip deficit. *Nature*, **435**(7040), 295–299

Goldstein RM and Werner CL (1998) Radar interferogram filtering for geophysical applications. *Geophys. Res. Lett.*, **25**(21), 4035–4038

Haug AJ (2012) *Bayesian estimation and tracking: a practical guide*. John Wiley & Sons

Houghton J and 7 others (2001) IPCC 2001: climate change 2001. *The Climate Change Contribution of Working Group I to the Third Assessment Report of the Intergovemmental Panel on Climate Change*, **159**

Howat IM, Joughin I, Fahnestock M, Smith BE and Scambos TA (2008) Synchronous retreat and acceleration of southeast Greenland outlet glaciers 2000–06: ice dynamics and coupling to climate. *J. Glaciol.*, **54**(187), 646–660

Huang H, Dabiri D and Gharib M (1997) On errors of digital particle image velocimetry. *Meas. Sci. Technol.*, **8**(12), 1427

Joughin I, Kwok R and Fahnestock M (1998) Interferometric estimation of three-dimensional ice-flow using ascending and descending passes. *IEEE Trans. Geosci. Remote Sens.*, **36**(1), 25–37 (doi: 10.1109/36.655315), ISSN 0196-2892

Joughin I and 7 others (2008) Continued evolution of Jakobshavn Isbrae following its rapid speedup. *J. Geophys. Res.: Earth*

Surf., **113**, f04006 (doi: 10.1029/2008JF001023), ISSN 2156-2202

Lhermitte RM and Miller LJ (1970) Doppler radar methodology for the observation of convective storms. In *Preprints*, 14*th Conference on Radar Meteorology, Tucson, AZ, American Meteor Society*, 133–138

Nettles M and 9 others (2008) Step-wise changes in glacier flow speed coincide with calving and glacial earthquakes at Helheim Glacier, Greenland. *Geophys. Res. Lett.*, **35**(24)

Peters IR and 6 others (2015) Dynamic jamming of iceberg-choked fjords. *Geophys. Res. Lett.*, **42**(4), 1122–1129

Strozzi T, Werner C, Wiesmann A and Wegmuller U (2012) Topography mapping with a portable real-aperture radar interferometer. *IEEE Geosci. Remote Sens. Lett.*, **9**(2), 277–281

Taylor ZJ, Gurka R, Kopp GA and Liberzon A (2010) Long-duration time-resolved PIV to study unsteady aerodynamics. *IEEE Trans. Instrum. Meas.*, **59**(12), 3262–3269

Voytenko D and 7 others (2015a) Multi year observations of Breidamerkurjökull, a marine-terminating glacier in southeastern Iceland, using terrestrial radar interferometry. *J. Glaciol.*, **61**(225), 42–54

Voytenko D and 5 others (2015b) Observations of inertial currents in a lagoon in southeastern Iceland using terrestrial radar interferometry and automated iceberg tracking. *Comput. Geosci.*, **82**, 23–30

Voytenko D and 5 others (2015c) Tidally driven ice speed variation at Helheim Glacier, Greenland, observed with terrestrial radar interferometry. *J. Glaciol.*, **61**(226), 301

Werner C, Strozzi T, Wiesmann A and Wegmüller U (2008) Gamma's portable radar interferometer. In *Proceedings of IAG/FIG*, Lisbon, Portugal

Xie S and 5 others (2016) Precursor motion to iceberg calving at Jakobshavn Isbræ, Greenland, observed with terrestrial radar interferometry. *J. Glaciol.*, **62**(236), 1134–1142

MS received 9 October 2016 and accepted in revised form 8 May 2017; first published online 6 June 2017